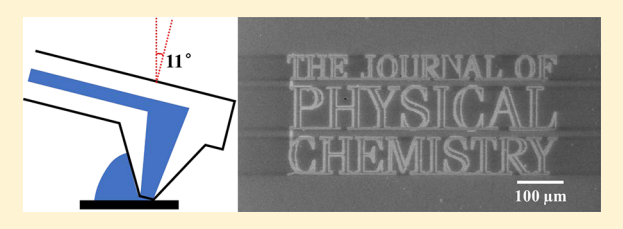
# Three-Dimensional Nanoprinting via Direct Delivery

Joao Ventrici de Souza, <sup>†</sup> Yang Liu, <sup>†</sup> Shuo Wang, <sup>†</sup> Pablo Dörig, <sup>‡</sup> Tonya L. Kuhl, <sup>§</sup> Jane Frommer, <sup>||</sup> and Gang-vu Liu\*,†@

ABSTRACT: Direct writing methods are a generic and simple means to produce designed structures in three dimensions (3D). The printing is achieved by extruding printing materials through a nozzle, which provides a platform to deliver a wide range of materials. Although this method has been routinely used for 3D printing at macroscopic scales, miniaturization to micrometer and nanometer scales and building hierarchical structures at multidimensional scales represent new challenges in research and development. The current



work addresses these challenges by combining the spatial precision of atomic force microscopy (AFM) and local delivery capability of microfluidics. Specialized AFM probes serve dual roles of a microscopy tip and a delivery tool, enabling the miniaturization of 3D printing via direct material delivery. Stacking grids of 20 µm periodicity were printed layer-by-layer covering 1 mm × 1 mm regions. The spatial fidelity was measured to be several nanometers, which is among the highest in 3D printing. The results clearly demonstrate the feasibility of achieving high precision 3D nanoprinting with nanometer feature size and accuracy with practical throughput and overall size. This work paves the way for advanced applications of 3D hierarchical nanostructures.

#### 1. INTRODUCTION

In the fields of 3D writing and additive manufacturing, the direct delivery method produces 3D structures with feature sizes down to the micrometer scale. 1-14 Direct writing methods produce structures by the extrusion of ink in the fluid state through a nozzle, followed by curing to retain shape. The inks suitable for this method are often composed of particulate and polymeric materials that are suspended or dissolved in a liquid solvent. Alternatively, a solid ink can be delivered by heating, with the melted materials extruded and solidified. The advantages of direct delivery include applicability to a wide range of materials and simplicity. While 3D printing via direct delivery is becoming routine with millimeter precision, further miniaturization is challenging due to the high accuracy required for positioning and material delivery. Current research and development efforts have pushed the feature size to micrometers by using smaller injection systems and suitable materials that can solidify upon extrusion. <sup>2,3,5,6,9,15–19</sup> Further miniaturization is increasingly difficult because of the high accuracy required for both reproducible positioning and material delivery for intralayers and interlayers. Here, we report our approach for miniaturizing 3D printing which combines the high spatial precision of atomic force microscopy (AFM) with direct delivery capability of microfluidics, similar to approaches reported previously. <sup>2,4,6,16,19</sup> Designed structures were printed layer-by-layer with interlayer alignment reaching 4.5-6.3 nm over a 1 mm printing field. The results demonstrate control over instrumental performance and material behavior under nanometer confinement, and advance modern technological applications that benefit from 3D nanostructures, such as nanophotonics, <sup>20–23</sup> nanoelectronics, <sup>24,25</sup> micro- and nanofluidic devices, <sup>26–29</sup> new nanocomposite materials, <sup>15,30,31</sup> and tissue engineering. 32-34

## 2. EXPERIMENTAL SECTION

2.1. Materials and Supplies. Reagents were used without further purification. Sulfuric acid (95.0-98.0%) and hydrogen peroxide (30% aqueous solution) were purchased from EMD Chemicals (Gibbstown, NJ, U.S.A.). Gold slugs (99.999%) were purchased from Alfa Aesar (Ward Hill, MA, U.S.A.). Deionized and ultrapure water (18.2 MΩ·cm at 25 °C) was from a Milli-Q water system (EMD Millipore, Billerica, MA, U.S.A.). The direct write material—Loctite AA 349 (Henkel, Germany)—consists of a mixture of methacrylate esters that are often used as adhesives because of their polymerization upon exposure to UV radiation (~365 nm). This Loctite was selected because its room temperature viscosity, 6000-13 500 mPa·s (cP), is appropriate for our delivery platform and desired feature size. Substrates of  $1" \times 3"$  glass slides (Fisherfinest Premium, Fisher Scientific, Pittsburgh, PA, U.S.A.) were

Special Issue: Miquel B. Salmeron Festschrift

Received: July 17, 2017 Revised: November 6, 2017 Published: November 9, 2017

<sup>&</sup>lt;sup>†</sup>Department of Chemistry, University of California, Davis, California 95616, United States

<sup>&</sup>lt;sup>‡</sup>Cytosurge AG, Glattbrugg 8152, Switzerland

<sup>§</sup>Department of Chemical Engineering, University of California, Davis, California 95616, United States

IBM Almaden Research Center, San Jose, California 95120, United States

immersed in Piranha solution, which consisted of 3 parts of sulfuric acid to 1 part of hydrogen peroxide 30%, for 2 h. The clean glass slides were rinsed with Milli-Q water and dried under a flow of nitrogen for 5 min.

- **2.2. AFM-based Nanofluidic Device.** The printing process was performed using a FluidFM BOT (Cytosurge, Glattbrugg, Switzerland) containing an inverted optical microscope (IX-73, Olympus America, Center Valley, PA, U.S.A.). The printing was carried out with a FluidFM Nanopipette (CYPR/001511, Cytosurge, Glattbrugg, Switzerland) with a 300 nm opening. Hamilton 7000 series syringes, 1 μL (Hamilton, Reno, NV, U.S.A.), were used to deliver materials into the instrument's reservoir.
- **2.3. Scanning Electron Microscopy.** The hierarchical 3D structures produced were characterized by scanning electron microscopy (SEM). To avoid charging, a thin layer (4 nm) of gold was deposited onto the glass slide, coating the printed structures, using a high-vacuum evaporator (DV502-A, Denton Vacuum, Moorestown, NJ, U.S.A.), at a base pressure below  $2 \times 10^{-6}$  Torr and evaporation rate of 1.5 Å/s. SEM images were acquired on a Hitachi S-4100T FE-SEM (Hitachi High Technologies America, Inc., Pleasanton, CA, U.S.A.), with an accelerating voltage of 2 kV at 10  $\mu$ A.
- **2.4. Atomic Force Microscopy.** AFM images were acquired using a deflection type configuration (MFP-3D, Oxford Instrument, Santa Barbara, CA, U.S.A.). Probes (AC240-TS, Olympus America, Central Valley, PA, U.S.A.) of 1.7 N/m spring constant and 57 kHz resonant frequency were used to characterize the geometry and size of the printed structures. The driving frequency was set at the fundamental resonance of the cantilever, 57 kHz, and the damping was set at 40%. Image processing and display were performed using either the MFP-3D software developed on the Igor Pro 6.20 platform or Gwyddion (open source software, Czech Metrology Institute, Brno, Czech Republic).

### 3. RESULTS AND DISCUSSION

**3.1. AFM-based Nanofluidic Device for 3D Nanoprinting.** The printing process was carried out on an integrated AFM and microfluidic platform, FluidFM BOT, as illustrated in Figure 1A. AFM-microfluidics combination enabled 3D printing. The integration of FluidFM Bot system into AFM enabled multi-scale 3D printing. The precision movement stage was mounted onto an inverted optical microscope to monitor the position and delivery. The x,y-movement range is 240 mm × 74 mm, with a precision of 100 nm; the z-movement is independent from lateral movement

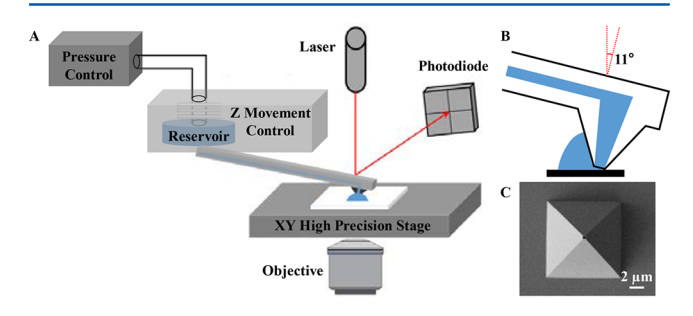


**Figure 1.** (A) Schematic diagram of the key parts of the combined AFM with microfluidics for 3D nanoprinting. (B) Schematic diagram of a microfluidic AFM cantilever and tip in contact with a surface. (C) SEM image of an actual tip apex revealing the 300 nm opening.

with 4 nm precision over 50 mm. The substrate for the 3D nanostructure was placed on the xy-stage, while the probe was mounted to the vertical assembly controlling z-movement. The AFM probes used for printing differ from conventional microfabricated AFM probes by having integrated microfluidic delivery. Typical probe-surface contact during delivery is shown in Figure 1B, where the contact force was measured and controlled via similar means as conventional AFM with a deflection configuration. The square pyramidal tip tilts 11° from the surface normal. The cantilever was similar to typical AFM silicon probes, 200  $\mu$ m long, 36  $\mu$ m wide, and 1.5  $\mu$ m thick. The spring constant was 2 N/m. The pyramidal tip had a square base with a side length of 10  $\mu$ m, and was 7  $\mu$ m in height. Important to material delivery, a 300 nm diameter pore was located at the apex and connected to a microchannel within (Figure 1C). The microchannel was connected to a small reservoir where the printing materials reside, and a mechanical pump and control system enabled application of pressures from -800 mbar to +1000 mbar with 1 mbar precision.

Prior to nanoprinting designed 3D structures, the material delivery characteristics of this instrument were tested by printing two basic geometries: droplet and line. More complex geometries, such as cuboids and pyramids, were then printed from a combination of the two basic geometries. Experimental parameters influencing the material delivery include probe and opening geometry and size, printing direction, pressure, speed, time, number of passes, environment, such as humidity, and surface functionality.

Under ambient conditions, droplet delivery to glass surfaces was first tested at various contact times. The process was highly automated and each droplet was delivered by approaching the probe from 5  $\mu$ m above the surface at 10  $\mu$ m/s until reaching a set contact force, e.g., 20 nN. The probe-surface contact was maintained at the set force for a designated time, after which the probe was withdrawn at 10  $\mu$ m/s until 5  $\mu$ m above the surface. We found that the amount of material delivered per droplet depended on the probe as the exit pore size and geometry varied slightly from probe-to-probe, even among the same type of probes. Thus, we recommend this basic test whenever the probe is changed. Figure 2 shows one example of such a droplet test where the cones formed upon curing were characterized via AFM. The amount of delivered material, as measured by the cone height and diameter (defined as full width at half-maximum, fwhm), increased with the contact time under constant pressure, e.g., 200 mbar, as summarized in

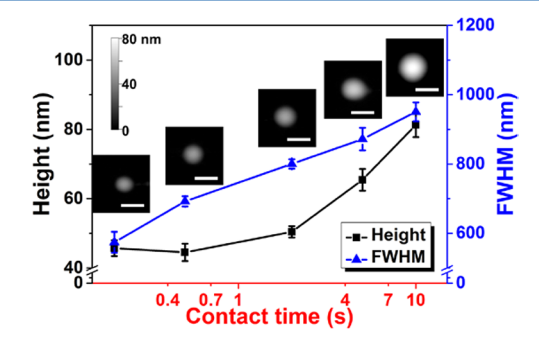


**Figure 2.** Height and fwhm of cones as a function of logarithm of the contact time. Insets are AFM images of the cones printed under the corresponding conditions. AFM imaging conditions: tapping mode at 57 kHz, 40% damping, scanning rate =  $26.03 \ \mu m/s$ . Scale bar is  $1 \ \mu m$ .

Table 1. These tests served as a guide for determining delivery conditions for printing cone features in 3D structures.

Table 1. Consolidated Parameters and Metrics for Single Point Delivery

contact time	pressure	force	height	diameter
(s)	(mbar)	(nN)	(nm)	(nm)
0.2	200	20	$45.7 \pm 2.3$	$574 \pm 30$
0.5			$44.5 \pm 2.5$	$692 \pm 15$
2			$50.4 \pm 1.4$	$801 \pm 14$
5			$65.4 \pm 3.2$	$872 \pm 33$
10			$81.3 \pm 3.5$	$951 \pm 27$

While cone features can be printed consistently via single point delivery, direction dependence is found for 1D printing, e.g., line shaped features, due to the asymmetry at the tipsurface contact (Figure 3A). This asymmetry exhibits little impact on the delivery of droplets that reorganize into cone shapes controlled by surface tension when the probe retracts. In the case of lines, material delivery exhibits directional dependence as illustrated with 4 representative directions in Figure 3B. The scanning direction parallel to the cantilever's long axis and on the tip face opposite to where the material exits is defined as 90°; the scanning direction parallel to the cantilever's long axis and on the same face of the tip as the exiting material is defined as 270°. The two directions perpendicular to the long axis are called 0° and 180°. Figure 3B shows printed line arrays on a glass surface along the 4 representative directions, each in a single pass. The heights of these lines measured 15.1  $\pm$  0.5, 20.8  $\pm$  0.4, 15.5  $\pm$  0.3, and 2.4  $\pm$  0.3 nm along the printing directions of 0, 90, 180, and 270°, respectively. This observation is consistent with expectations from the geometry of the probe-surface contact: there is little perturbation of the printed line by the tip in the case of lines printed in the 90° scan direction, while the tip directly sweeps through the just delivered material in the case of 270°, thus hampering material delivery and producing smaller line heights.

Dependence on printing speed and number of passes was also investigated and the results, in conjunction with directional dependence, are summarized in Table 2. As the printing speed increased from 20 to 420  $\mu$ m/s, the line width decreased from 456  $\pm$  18 to 306  $\pm$  12 nm and the height decreased from 14.5  $\pm$  0.3 to 8.3  $\pm$  0.2 nm.

Retracing a line at designed number of passes allows material build-up along surface normal. A single pass produced lines of  $14.6 \pm 0.2$  nm height. Retracing atop this line under the same conditions increased in height by 3 nm/pass, as shown in

Figure 3C and Table 2. It is not uncommon for the amount of material delivered in the first layer to differ from subsequent layers, as the material-surface interactions differ from material-material interactions.<sup>35–40</sup> The effect of pressure and contact force was also monitored from 20 to 420 mbar and from 10 to 50 nN, respectively. The material delivery, quantified by the line height and lateral dimension, remained unchanged within 10% under these pressure and force variations. These basic tests provide quantitative measurements of material delivery associated with specific probes, surfaces, materials, and environment. It is essential with each printing setup that these tests be performed prior to designing and printing 3D nanostructures in order to reach high fidelity.

3.2. Layer-by-Layer Printing of 3D Structures. To extend the feasibility of creating 3D structures with layer-bylayer delivery, we designed and constructed a simple 3-layered structure as shown in Figure 4. This type of design is widely regarded as a standard pattern for demonstrating 3D printing in the field of macroscale additive manufacturing. 11,13,41 Printing was carried out at 20 nN contact force following 0° scanning direction, under an extrusion pressure of 200 mbar, and a printing speed of 50  $\mu$ m/s. The first layer was a cuboid with a square base of 20  $\mu$ m  $\times$  20  $\mu$ m, 27 nm tall, created with 81 lines at 250 nm spacing. The execution of this design was based on the basic tests discussed in Section 3.1 and Table 2, which predicted the width of each line would be 412 nm. Since the periodicity of 250 nm was smaller than the line width of 412 nm, and the polymer would not cure during the first several seconds after delivery, the nearest neighbor lines are expected to spread and connect, resulting in a solid cuboid, as confirmed in Figure 4. A second layer was deposited on top of the first layer with dimensions of 12  $\mu$ m  $\times$  12  $\mu$ m. It was composed from 31 lines printed at 400 nm periodicity to test the dependence of layer height on line density. The third layer consisted of 4 cones, one atop each quadrant in the second layer, spaced 5  $\mu$ m from each other and at 3  $\mu$ m from the center of the 2nd layer. The 4 cones were produced by dispensing a droplet with a contact time of 1 s under 200 mbar pressure and 20 nN contact force, as guided by the basic tests discussed in Section 3.1 and pictured in Figure 2. The 3D structure was exposed to 365 nm radiation at 40 mW/cm<sup>2</sup> for 15 min after each layer was deposited to ensure complete curing. AFM images were acquired after completion of each layer and are shown in Figure 4A - C. The decrease in height from  $27.0 \pm 1.9$  to  $19.7 \pm 2.1$  nm ongoing from the first to the second layer was attributed to a decrease in line density and the change in the receiving surface material mentioned above. The

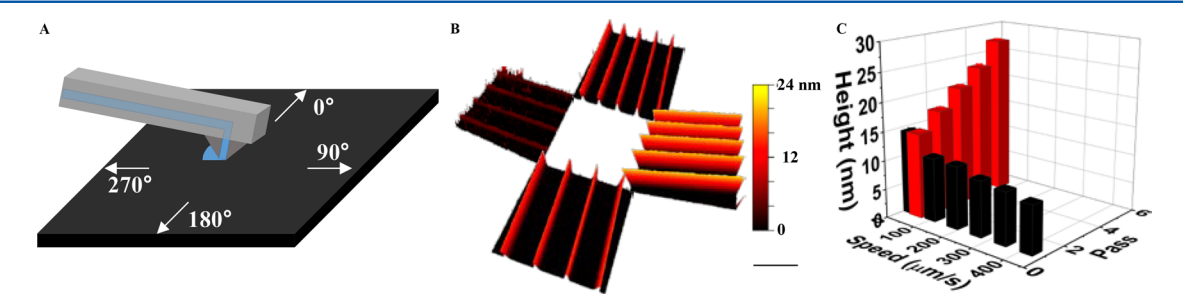


**Figure 3.** (A) Schematic diagram of 4 representative printing directions. (B) AFM images of 4 sets of parallel lines printed at the 4 directions as indicted in (A). Lateral scale bar = 5  $\mu$ m. (C) Height of printed lines plotted as a function of printing speed and number of passes under the 1D delivery condition presented. AFM imaging conditions: tapping mode at 57 kHz, 40% damping, scanning rate = 26.03  $\mu$ m/s.

The Journal of Physical Chemistry B

Table 2. Consolidated Parameters and Metrics from 1D Delivery

printing speed $(\mu m/s)$	printing direction (deg)	# of passes	pressure (mbar)	force (nN)	height (nm)	width as fwhm (nm)
50	0	1	200	20	$15.1 \pm 0.5$	$412 \pm 14$
50	90	1			$20.8 \pm 0.4$	$385 \pm 9$
50	180	1			$15.5 \pm 0.3$	$440\pm22$
50	270	1			$2.4 \pm 0.3$	$554 \pm 50$
20	0	1	200	20	$14.5 \pm 0.3$	$456 \pm 18$
100	0	1			$11.0 \pm 0.2$	$386 \pm 16$
180	0	1			$10.8 \pm 0.2$	$363 \pm 16$
260	0	1			$9.6 \pm 0.2$	$347 \pm 14$
340	0	1			$9.1 \pm 0.2$	$319 \pm 12$
420	0	1			$8.3 \pm 0.2$	$306 \pm 12$
50	0	1	200	20	$14.6 \pm 0.2$	$406 \pm 15$
50	0	2			$17.5 \pm 0.3$	$431 \pm 15$
50	0	3			$20.6 \pm 0.3$	$452 \pm 16$
50	0	4			$23.4 \pm 0.4$	$478 \pm 20$
50	0	5			$27.5 \pm 0.2$	$503 \pm 24$

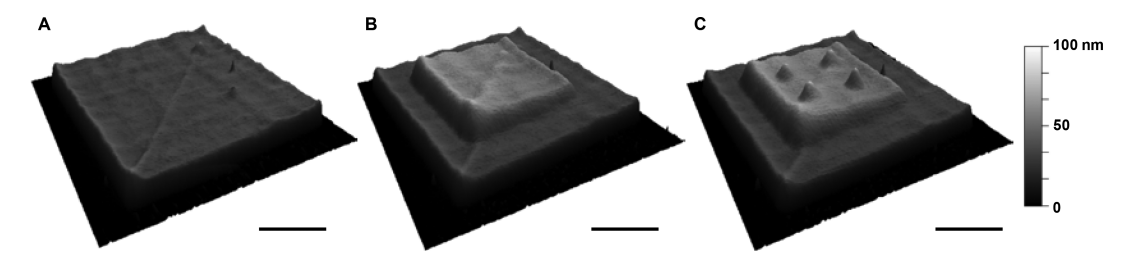


**Figure 4.** AFM topographic images of the 3-layer structure produced by printing (A) 1st layer cuboid, (B) 2nd layer cuboid, (C) 3rd layer of cones. Lateral scale bars are 5  $\mu$ m. AFM imaging conditions: tapping mode at 57 kHz, 40% damping, scanning rate = 50.01  $\mu$ m/s.

cone dimensions were measured 20.3  $\pm$  3.1 nm in height and 1125  $\pm$  14 nm in fwhm.

3.3. Determination of the Spatial Precision of 3D Nanoprinting. While nanometer precision has been reached using AFM-based technologies for 2D printing (i.e., in the x,yplane),41-46 reliable nm scale printing in the z-dimension is much more challenging due to difficulties in alignment and registry from one layer to another. The alignment and registry can tolerate only minimal drift with time. The multipass experiments of Section 3.1 demonstrate spatial accuracy when performing repeated line printing in a short time. To test the spatial accuracy in performing 3D nanoprinting by design, more complex structures need to be tested and the probe must be accurately positioned at designated locations atop the layer underneath. Toward this goal, 3-layered stacked grids were designed (Figure 5) and printed (Figure 6). A grid of an overall dimension of 1 mm × 1 mm was constructed on glass from a pattern of 51 lines at a periodicity of 20  $\mu$ m. The first and third layers shared the same design and positioning, thus the 51 lines of the third layer were superpositioned atop the 51 lines of the first layer. The 51 lines of the second (middle) layer were written perpendicular to the other two layers. Printing directions of 0° for layers 1 and 3 and 270° for layer 2 were used; with these writing orientations the lines of the first and third layers were expected to be taller than the lines of the second layer (Figure 3A and B). The heights of first and second layers were found to be 13 and 5 nm relative to the substrate, respectively, guided by the basic printing tests discussed in Section 3.1: 50  $\mu$ m/s printing speed, 200 mbar pressure, and 20 nN contact force. Given the solution's viscosity (6000-13500 mPa·s), and several seconds of drying time, the second layer's lines were expected to lie conformally over both the substrate

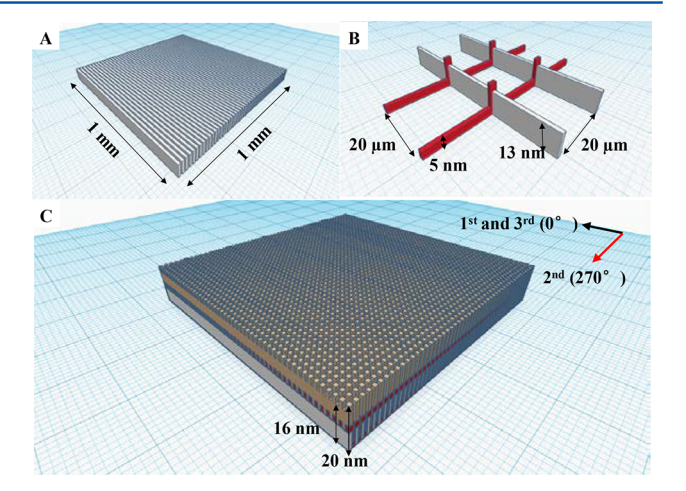


Figure 5. Schematic diagrams of the stacking grids. (A) The first layer establishes the overall layout of the 51 parallel lines at a periodicity of 20  $\mu$ m. The footprint (overall dimension) covers 1 mm  $\times$  1 mm. (B) The second layer (red) follows an identical periodicity, but the lines are perpendicular to those of the first layer. (C) The third layer (brown) follows the same periodicity and orientation as the first layer. The printing directions are indicated with the black (1st and 3rd layers) and red (2nd layer) arrows.

surface and the lines of layer 1, instead of being suspended in the air between the lines of layer 1 (like a clothesline). The second layer's lines displayed a height of 5 nm when in contact with the substrate, due to the less favorable printing direction. The third layer was deposited to lie conformally along every line of the first layer; as expected, the third layer's lines were not as tall as the first layer's line since the material solution-cured material interactions differ from the material solution-

The Journal of Physical Chemistry B

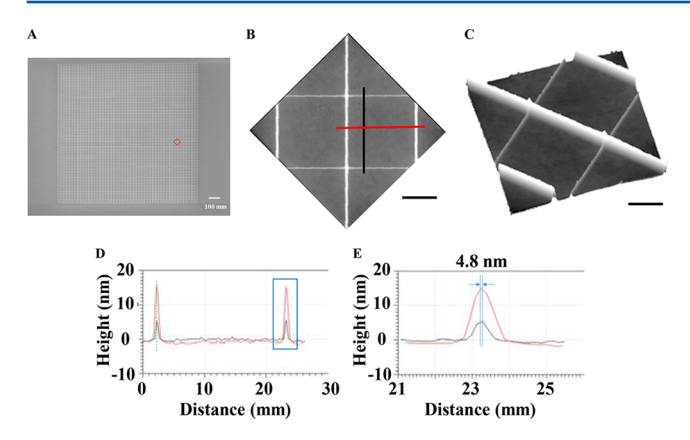


Figure 6. (A) A 1.1 mm  $\times$  1.4 mm SEM image showing the 3-layer grids printed following the design in Figure 5C. (B) A 40  $\mu m \times 40~\mu m$  AFM topographic image shows detail of the grid region as indicated by the red frame in (A). (C) 3D rendition of the AFM topography image (B). Scale bars in (B) and (C) are 10  $\mu m$ . (D) Combined profiles from the 2 cursors indicated in (B). (E) A zoom-in view of the right peak in (D) shows the center of adjacent grid lines are aligned with 4.8 nm precision. AFM imaging conditions: contact mode at 55 nN, scan rate is 30  $\mu m/s$ .

glass interactions. The third layer's line height was 3 nm, contributing to a total 3-layer height of 20 nm. At a printing speed of 50  $\mu$ m/s, the total time to complete each layer was 17 min, or 51 min to complete the entire 3D structure. The 3-layer structure was exposed to 365 nm radiation at 40 mW/cm² for 15 min to ensure complete curing. Therefore, the total time to construct the 1 mm × 1 mm grid structure was about 66 min.

The printed structures were characterized using SEM to visualize the overall structure and fidelity to design. Figure 6A is an SEM image displaying the overall pattern covering the entire 1 mm × 1 mm area. The stacked grids appear uniform over the entire region with little distortion or mis-position. A similar geometry with mm feature size was printed with hydrogel materials using conventional lithography.<sup>47</sup> The structures shown in our work demonstrate the feasibility to miniaturize feature size using our new approach. The AFM topography images in Figure 6B and C show the dimensions of the individual lines and periodicity. Along the grid, the lines' width and height is relatively homogeneous. The periodicity is 20  $\mu$ m in both directions. The cursor profiles, indicated in black and red lines in Figure 6B, are displayed in Figure 6D. The 2 lines in the second layer (black cursor) are 5.0 and 6.0 nm high, and 310 and 330 nm wide (fwhm), respectively. The 2 lines in the combined first and third layers (red cursor) measure 16.0 nm in height, and 680 and 740 nm in width. The measurements shown in Figure 6 were highly reproducible within the same experiment, as 5 locations were randomly selected and measured via AFM imaging. In addition, four independent experiments were performed on 4 surfaces using the same design, which yielded consistently 4.8-6.0 nm in height and 310-370 nm in width when printing the second layer. The height and width of the combined first and third layer lines measured 14.0-17.0 nm and 490-740 nm, respectively. By producing features on a length scale of nanometers over a field of millimeters, this study demonstrates high reproducibility and consistency for producing 3D structures with practical sizes for further applications.

AFM images provide information about the precision of the interline spacing throughout the 3D nanostructure. Figure 6D

superimposes two cross-sectional profiles to compare the interline spacing of different layers. The red cursor was drawn over 2 stacked lines from the first and third layers to measure the offset between the first and third layers. Figure 6E expands the x-axis of Figure 6D to illustrate that nearest neighbor grid lines are positioned with 4.8 nm accuracy. This repeatable positional accuracy is remarkable when considered in the context of lateral instrumental drift. Nearest neighbor line spacing was measured at 5 different locations throughout the 3D structure, from the central region to the corner, yielding a statistical alignment precision of 4.5-6.3 nm. To the best of our knowledge, this level of spatial accuracy over a field of 1 mm is among the highest reported in 3D printing. These results of consistent and high spatial precision demonstrate that 3D nanoprinting of structures for practical applications is now achievable, paving the way for more advanced applications in areas such as devices, tissue engineering and cellular biology.

**3.4.** Extension of 3D Nanoprinting from Rectilinear to Complex Structures. A four-leaf clover structure was chosen to demonstrate the ability to produce 3D structures that deviate from the previous rectilinear designs, replicating the structure at 7 different sizes. The outline of the leaf was made in 3 passes, layer-by-layer, along lateral dimensions marked as a and b (Figure 7). Seven clovers were printed with seven sets of a and b values, all at the same aspect ratio of a:b=1.15:1, summarized in Table 3.

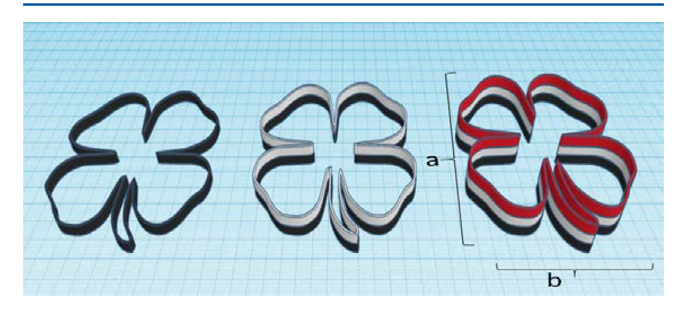


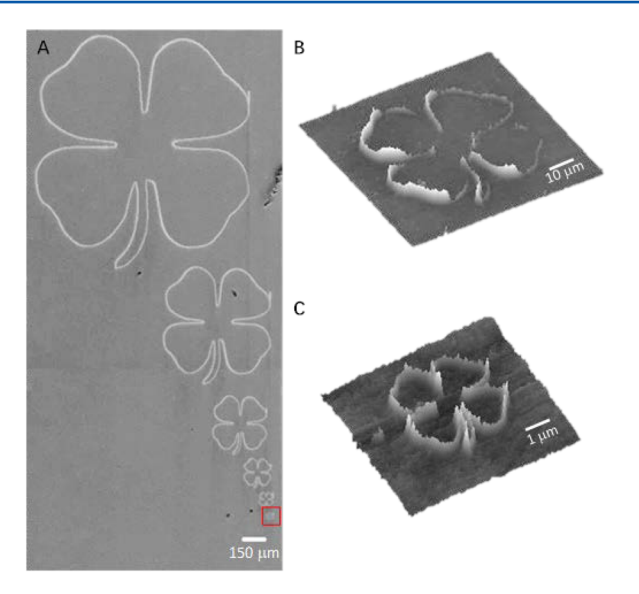
Figure 7. Schematic diagram for the printing of four-leaf clovers in three stacked passes.

Table 3. Summary of the Lateral Dimensions of the 7 Printed Clovers Following the Design Shown in Figure 7

index	a (μm)	b (μm)
1	1500.0	1300.0
2	750.0	650.0
3	375.0	325.0
4	190.0	165.0
5	95.0	82.0
6	50.0	43.0
7	5.00	4.30

A clover drawing was converted into XY values using ImageJ software. The comma-separated value (CSV) file of XY positions, together with parameters for printing speed and pressure, were uploaded to the instrument data acquisition software to direct the printing processes.

At a printing speed of 50  $\mu$ m/s for clovers #1–6 and 5  $\mu$ m/s for clover #7, the 7 features were printed in 13.3 min. The SEM image in Figure 8A shows clovers 1–6 with only a small degree of distortion or fuzziness of the lines. The largest leaf ( $a = 1500 \mu$ m and  $b = 1300 \mu$ m) had a line width of 0.45  $\mu$ m, indicating good alignment of the three stacked layers. Clover #6, not



**Figure 8.** (A) SEM image of clovers #1–6. (B) 3D display of an AFM topographic image of clover #6, surrounded by the red frame in (A). (C) 3D display of an AFM topographic image of the smallest clover #7. AFM images were acquired using contact mode imaging under 55 nN.

clearly resolved under SEM , was imaged by AFM (Figure 8B) to reveal line widths (fwhm) of  $0.31-0.47~\mu m$ , line heights of 1.4-11.0~nm, and left line edges systematically higher than right line edges. This asymmetric line profile is due to the directional dependence of the printing configuration as discussed in Section 3.1. This heterogeneity could be partially remedied using slower printing speeds or less viscous ink. The smallest feature, clover #7 with  $a = 5~\mu m$ ,  $b = 4.3~\mu m$ , displayed the narrowest line width of  $0.13~\mu m$  and a height of 3.1~nm. The structures printed in Figure 8 demonstrate that this 3D nanoprinting method allows the construction of complex designs beyond rectilinear geometries, essential in advanced applications for constructing nanodevices and matrices for tissue engineering.

## CONCLUSION

This work reports 3D nanoprinting using combined scanning probe microscopy and microfluidic technologies. The combination takes advantage of both technologies: scanning probe microscopy to reach high spatial precision and accuracy, and microfluidics to enable precise control over material delivery. This approach enabled printing of 3D nanostructures following custom designs, e.g. stacking line grids, space-filled geometries, and rounded structures. Multiscale hierarchical 3D printing has become a reality, illustrated in our creation of nm features to mm overall structure size. The in-plane spatial precision and vertical layer-by-layer deposition achieved  $5.5 \pm 1$  nm precision over 1 mm areas. Work is in progress to further optimize material formulation and printing conditions to enable further miniaturization of feature size. This approach also facilitates progress in physical chemistry of materials under nanometer confinement.

The method of direct material delivery is promising for developing a generic platform for 3D nanoprinting of a wide range of materials and advances technological applications including nanodevices, tissue engineering, micro- and nanofluidics, and new nanocomposite materials.

#### AUTHOR INFORMATION

#### **Corresponding Author**

\*Phone: (530) 754-9678; Fax: (530) 754-8557; E-mail: gyliu@ucdavis.edu.

#### ORCID

Jane Frommer: 0000-0002-5198-6127 Gang-yu Liu: 0000-0003-3689-0685

#### Notes

The authors declare no competing financial interest.

#### ACKNOWLEDGMENTS

We thank Mr. William Deng for his assistance in preparing illustrations, Ms. Jiali Zhang for helpful discussions, and Ms. Susan Stagner for careful proof-reading of the article. We thank both reviewers for their careful reading of the article and their critiques, which significantly improve the clarity and quality of this article. We gratefully acknowledge the support from the Gordon and Betty Moore Foundation and the National Science Foundation (CHE-1413745). J.V. is supported in part by Conselho Nacional de Desenvolvimento Cientifico e Tecnologico (Brazilian National Council for Scientific and Technological Development). Y.L. is supported by UCD-LLNL Joint Graduate Student Mentorship Award.

#### REFERENCES

- (1) Zhang, X.; Jiang, X. N.; Sun, C. Micro-stereolithography of polymeric and ceramic microstructures. *Sens. Actuators, A* **1999**, 77, 149–156.
- (2) Fang, A. P.; Dujardin, E.; Ondarcuhu, T. Control of droplet size in liquid nanodispensing. *Nano Lett.* **2006**, *6*, 2368–2374.
- (3) Gratson, G. M.; Xu, M.; Lewis, J. A. Direct writing of three-dimensional webs. *Nature* **2004**, 428, 386.
- (4) Loh, O.; Lam, R.; Chen, M.; Moldovan, N.; Huang, H. J.; Ho, D.; Espinosa, H. D. Nanofountain-probe-based high-resolution patterning and single-cell injection of functionalized nanodiamonds. *Small* **2009**, *5*, 1667–1674.
- (5) Therriault, D.; Shepherd, R. F.; White, S. R.; Lewis, J. A. Fugitive inks for direct-write assembly of three-dimensional microvascular networks. *Adv. Mater.* **2005**, *17*, 395–399.
- (6) Meister, A.; Liley, M.; Brugger, J.; Pugin, R.; Heinzelmann, H. Nanodispenser for attoliter volume deposition using atomic force microscopy probes modified by focused-ion-beam milling. *Appl. Phys. Lett.* **2004**, *85*, 6260–6262.
- (7) Ahn, B. Y.; Duoss, E. B.; Motala, M. J.; Guo, X.; Park, S.-I.; Xiong, Y.; Yoon, J.; Nuzzo, R. G.; Rogers, J. A.; Lewis, J. A. Omnidirectional printing of flexible, stretchable, and spanning silver microelectrodes. *Science* **2009**, 323, 1590–1593.
- (8) Schaedler, T. A.; Jacobsen, A. J.; Torrents, A.; Sorensen, A. E.; Lian, J.; Greer, J. R.; Valdevit, L.; Carter, W. B. Ultralight metallic microlattices. *Science* **2011**, *334*, 962–965.
- (9) Zheng, X.; Smith, W.; Jackson, J.; Moran, B.; Cui, H.; Chen, D.; Ye, J.; Fang, N.; Rodriguez, N.; Weisgraber, T.; et al. Multiscale metallic metamaterials. *Nat. Mater.* **2016**, *15*, 1100–1107.
- (10) Rohrig, M.; Thiel, M.; Worgull, M.; Holscher, H. 3D direct laser writing of nano- and microstructured hierarchical gecko-mimicking surfaces. *Small* **2012**, *8*, 3009–3015.
- (11) Ivanova, O.; Williams, C.; Campbell, T. Additive manufacturing (AM) and nanotechnology: promises and challenges. *Rapid Prototyp. J.* **2013**, *19*, 353–364.
- (12) Jang, D.; Meza, L. R.; Greer, F.; Greer, J. R. Fabrication and deformation of three-dimensional hollow ceramic nanostructures. *Nat. Mater.* **2013**, *12*, 893–898.
- (13) Frazier, W. E. Metal additive manufacturing: a review. J. Mater. Eng. Perform. 2014, 23, 1917–1928.

- (14) Farahani, R. D.; Chizari, K.; Therriault, D. Three-dimensional printing of freeform helical microstructures: A review. *Nanoscale* **2014**, *6*, 10470–10485.
- (15) Compton, B. G.; Lewis, J. A. 3D-printing of lightweight cellular composites. *Adv. Mater.* **2014**, *26*, 5930–5935.
- (16) Gruter, R. R.; Voros, J.; Zambelli, T. FluidFM as a lithography tool in liquid: spatially controlled deposition of fluorescent nanoparticles. *Nanoscale* **2013**, *5*, 1097–1104.
- (17) Meister, A.; Gabi, M.; Behr, P.; Studer, P.; Voros, J.; Niedermann, P.; Bitterli, J.; Polesel-Maris, J.; Liley, M.; Heinzelmann, H.; et al. FluidFM: Combining atomic force microscopy and nanofluidics in a universal liquid delivery system for single cell applications and beyond. *Nano Lett.* **2009**, *9*, 2501–2507.
- (18) Hirt, L.; Reiser, A.; Spolenak, R.; Zambelli, T. Additive manufacturing of metal structures at the micrometer scale. *Adv. Mater.* **2017**, 29, 1604211.
- (19) Hirt, L.; Ihle, S.; Pan, Z. J.; Dorwling-Carter, L.; Reiser, A.; Wheeler, J. M.; Spolenak, R.; Voros, J.; Zambelli, T. Template-free 3D microprinting of metals using a force-controlled nanopipette for layer-by-layer electrodeposition. *Adv. Mater.* **2016**, *28*, 2311–2315.
- (20) Yablonovitch, E. Inhibited spontaneous emission in solid-state physics and electronics. *Phys. Rev. Lett.* **1987**, *58*, 2059–2062.
- (21) Joannopoulos, J. D.; Villeneuve, P. R.; Fan, S. Photonic crystals: Putting a new twist on light. *Nature* **1997**, *386*, 143–149.
- (22) Lin, S. Y.; Fleming, J. G.; Hetherington, D. L.; Smith, B. K.; Biswas, R.; Ho, K. M.; Sigalas, M. M.; Zubrzycki, W.; Kurtz, S. R.; Bur, J. A three-dimensional photonic crystal operating at infrared wavelengths. *Nature* 1998, 394, 251–253.
- (23) Yablonovitch, E. Photonic crystals: semiconductors of light. *Sci. Am.* **2001**, 285, 46–55.
- (24) Nagel, R. D.; Haeberle, T.; Schmidt, M.; Lugli, P.; Scarpa, G. Large area nano-transfer printing of sub-50-nm metal nanostructures using low-cost semi-flexible hybrid templates. *Nanoscale Res. Lett.* **2016**, *11*, 143–151.
- (25) Melinte, G.; Moldovan, S.; Hirlimann, C.; Liu, X.; Begin-Colin, S.; Begin, D.; Banhart, F.; Pham-Huu, C.; Ersen, O. Towards nanoprinting with metals on graphene. *Nat. Commun.* **2015**, *6*, 8071–8078.
- (26) Pi, H.; Tong, J.; Bian, C.; Xia, S. 3D printed micro/nanofluidic preconcentrator for charged sample based on ion concentration polarization. *J. Micromech. Microeng.* **2017**, 27, 055008–055015.
- (27) Park, J.; Kim, K.; Kim, K.; Kim, D.; Cho, D.; Lee, J. H.; Jeon, S. Rapid, high-resolution 3D interference printing of multilevel ultralong nanochannel arrays for high throughput nanofluidic transport. *Adv. Mater.* **2015**, 27, 8000–8006.
- (28) Yazdi, A. A.; Popma, A.; Wong, W.; Nguyen, T.; Pan, Y. Y.; Xu, J. 3D printing: an emerging tool for novel microfluidics and lab-on-a-chip applications. *Microfluid. Nanofluid.* **2016**, *20*, 18.
- (29) Bhattacharjee, N.; Urrios, A.; Kang, S.; Folch, A. The upcoming 3D-printing revolution in microfluidics. *Lab Chip* **2016**, *16*, 1720–1742.
- (30) Chai, G. S.; Yoon, S. B.; Yu, J.-S.; Choi, J.-H.; Sung, Y.-E. Ordered porous carbons with tunable pore sizes as catalyst supports in direct methanol fuel cell. *J. Phys. Chem. B* **2004**, *108*, 7074–7079.
- (31) Zheng, X.; Lee, H.; Weisgraber, T. H.; Shusteff, M.; DeOtte, J.; Duoss, E. B.; Kuntz, J. D.; Biener, M. M.; Ge, Q.; Jackson, J. A.; et al. Ultralight, ultrastiff mechanical metamaterials. *Science* **2014**, 344, 1373–1377.
- (32) Mandrycky, C.; Wang, Z. J.; Kim, K.; Kim, D. H. 3D bioprinting for engineering complex tissues. *Biotechnol. Adv.* **2016**, *34*, 422–434.
- (33) Gao, G. F.; Cui, X. F. Three-dimensional bioprinting in tissue engineering and regenerative medicine. *Biotechnol. Lett.* **2016**, 38, 203–211.
- (34) Lee, J. W. 3D nanoprinting technologies for tissue engineering applications. *J. Nanomater.* **2015**, 2015, 1.
- (35) Wang, J. M.; Huang, C. P.; Allen, H. E.; Cha, D. K.; Kim, D. W. Adsorption characteristics of dye onto sludge particulates. *J. Colloid Interface Sci.* 1998, 208, 518–528.

- (36) Lvov, Y.; Decher, G.; Mohwald, H. Assembly, structural characterization, and thermal-behavior of layer-by-layer deposited ultrathin films of poly(vinyl sulfate) and poly(allylamine). *Langmuir* 1993, 9, 481–486.
- (37) Decher, G.; Hong, J. D. Buildup of ultrathin multilayer films by a self-assembly process 0.1. Consecutive adsorption of anionic and cationic bipolar amphiphiles on charged surfaces. *Makromol. Chem., Macromol. Symp.* **1991**, *46*, 321–327.
- (38) Decher, G.; Hong, J. D. Buildup of ultrathin multilayer films by a self-assembly process 0.2. Consecutive adsorption of anionic and cationic bipolar amphiphiles and polyelectrolytes on charged surfaces. Berichte Der Bunsen-Gesellschaft-Physical Chemistry Chemical Physics 1991, 95, 1430–1434.
- (39) Schlenoff, J. B.; Dubas, S. T. Mechanism of polyelectrolyte multilayer growth: Charge overcompensation and distribution. *Macromolecules* **2001**, *34*, 592–598.
- (40) Scheufele, F. B.; Modenes, A. N.; Borba, C. E.; Ribeiro, C.; Espinoza-Quinones, F. R.; Bergamasco, R.; Pereira, N. C. Monolayer-multilayer adsorption phenomenological model: Kinetics, equilibrium and thermodynamics. *Chem. Eng. J.* **2016**, 284, 1328–1341.
- (41) Liu, G.-Y.; Xu, S.; Qian, Y. Nanofabrication of self-assembled monolayers using scanning probe lithography. *Acc. Chem. Res.* **2000**, 33, 457–466.
- (42) Xu, S.; Liu, G.-y. Nanometer-scale fabrication by simultaneous nanoshaving and molecular self-assembly. *Langmuir* **1997**, *13*, 127–129.
- (43) Liu, G. Y.; Amro, N. A. Positioning protein molecules on surfaces: A nanoengineering approach to supramolecular chemistry. *Proc. Natl. Acad. Sci. U. S. A.* **2002**, *99*, 5165–5170.
- (44) Yang, G. H.; Amro, N. A.; Liu, G. Y. Scanning probe lithography of self-assembled monolayers. In *Nanofab. Technol.*, Dobisz, E. A., Ed.; 2003; Vol. 5220, pp 52–65.
- (45) Zhao, J. L.; Swartz, L. A.; Lin, W. F.; Schlenoff, P. S.; Frommer, J.; Schlenoff, J. B.; Liu, G. Y. Three-dimensional nanoprinting via scanning probe lithography-delivered layer-by-layer deposition. *ACS Nano* **2016**, *10*, 5656–5662.
- (46) Shim, W.; Braunschweig, A. B.; Liao, X.; Chai, J. N.; Lim, J. K.; Zheng, G. F.; Mirkin, C. A. Hard-tip, soft-spring lithography. *Nature* **2011**, 469, 516–521.
- (47) Hahn, M. S.; Taite, L. J.; Moon, J. J.; Rowland, M. C.; Ruffino, K. A.; West, J. L. Photolithographic patterning of polyethylene glycol hydrogels. *Biomaterials* **2006**, *27*, 2519–2524.